Spatial Analysis of 3′ Phosphoinositide Signaling in Living Fibroblasts, III: Influence of Cell Morphology and Morphological Polarity

Ian C. Schneider, Elizabeth M. Parrish, and Jason M. Haugh
Department of Chemical & Biomolecular Engineering, North Carolina State University, Raleigh, North Carolina

ABSTRACT Activation of phosphoinositide (PI) 3-kinase is a required signaling pathway in fibroblast migration directed by platelet-derived growth factor. The pattern of 3′ PI lipids in the plasma membrane, integrating local PI 3-kinase activity as well as 3′ PI diffusion and turnover, influences the spatiotemporal regulation of the cytoskeleton. In fibroblasts stimulated uniformly with platelet-derived growth factor, visualized using total internal reflection fluorescence microscopy, we consistently observed localized regions with significantly higher or lower 3′ PI levels than adjacent regions (hot and cold spots, respectively). A typical cell contained multiple hot spots, coinciding with apparent leading edge structures, and at most one cold spot at the rear. Using a framework for finite-element modeling with actual cell contact area geometries, we find that although the 3′ PI pattern is affected by irregular contact area shape, cell morphology alone cannot explain the presence of hot or cold spots. Our results and analysis instead suggest that these regions reflect different local 3′ PI dynamics, specifically through a combination of mechanisms: enhanced PI 3-kinase activity, reduced 3′ PI turnover, and possibly slow/constrained 3′ PI diffusion. The morphological polarity of the cell may thus bias 3′ PI signaling to promote persistent migration in fibroblasts.

INTRODUCTION

Directed cell migration, or taxis, is an important phenomenon encountered in the innate immune response, wound healing, and other physiological and pathological processes. In wound healing, invasion of fibroblasts into the fibrin clot is significantly accelerated through their ability to sense and migrate toward gradients of soluble platelet-derived growth factor (PDGF), produced by platelets, macrophages, and other cell types in the clot (1,2). PDGF isoforms bind and induce dimerization of specific cell surface receptors, members of the receptor tyrosine kinase family. Dimerized PDGF receptors recruit and activate a host of cytoplasmic signaling proteins and protein complexes (3,4). One such complex, the heterodimeric phosphoinositide (PI) 3-kinase, is robustly activated by PDGF receptors and is an established requirement for membrane motility processes in fibroblasts and other cell/receptor systems (5–10).

Type I PI 3-kinases phosphorylate phosphatidylinositol (PtdIns) (4,5)-bisphosphate [PtdIns(4,5)P_2], a lipid found in the inner leaflet of the plasma membrane, on the 3′ position of the inositol ring (11,12). The product, PtdIns(3,4,5)P_3, and its derivative PtdIns(3,4)P_2 (collectively referred to as 3′ PIs), interact with specific signaling proteins and mediate pathways known to be responsible for modulation of the cytoskeleton, such as activation of the Rho family GTPases Rac and Cdc42 (13,14). Moreover, external chemoattractant gradients elicit polarized 3′ PI patterns in numerous cell types, including fibroblasts (8,15,16). Hence, a conceptual model has emerged in which gradient-sensing in eukaryotes is based on the spatially localized activation of cell surface receptors and PI 3-kinase and production of 3′ PI lipid second messengers (17–19). A prerequisite for spatial gradient sensing is that the range of the second messenger, defined by its relative diffusion and turnover rates, must be sufficiently small relative to cellular dimensions (8,20). To estimate these and other parameters quantitatively for many cells, we previously analyzed the kinetics and pattern of 3′ PIs in mouse fibroblasts stimulated uniformly with PDGF (21,22). The restriction of PDGF-stimulated PI 3-kinase activity to the nonadherent portion of the plasma membrane in our cells produces a spatial 3′ PI pattern, and the spatiotemporal response was characterized through direct comparison of results obtained from mathematical modeling and live-cell total internal reflection fluorescence (TIRF) microscopy experiments. The model equations were calculated on a hemispherical surface approximating the cell membrane.

Although this model gave good agreement with measured fluorescence profiles across the center of the contact area, it was anticipated that certain local regions of the membrane might exhibit 3′ PI levels that deviate from the model (21). This conjecture was based on our observation that certain localized regions of the contact area show significantly higher or lower fluorescence intensities relative to adjacent regions; such regions are referred to here as *hot spots* or *cold spots*, respectively. It was further recognized that a more realistic model of the cell geometry would be needed to account for the effect of cell shape on the 3′ PI pattern in the contact area.

How might such hot and cold spots arise? It is clear that the cytoskeleton is not only a target for receptor-mediated signaling, but also a signaling mediator in its own right. Morphological polarization is a general characteristic of

Submitted February 15, 2005, and accepted for publication May 23, 2005.

Address reprint requests to Jason M. Haugh, Box 7905, North Carolina State University, Raleigh, NC 27695. Tel.: 919-513-3851; Fax: 919-515-3465; E-mail: jason_haugh@ncsu.edu.

0006-3495/05/08/1420/11 $2.00
doi: 10.1529/biophysj.105.061218

migrating cells and is seen dramatically at the free edges of ''wounded'' fibroblast monolayers. An actin-rich leading edge is formed, with one or more protruding lamellipodia and long, thin filopodia, accompanied by translocation of the microtubule organizing center and orientation of microtubules toward the leading edge (14,23,24). Fibroblast polarization also enriches 3′ PI lipids at the leading edge, in the absence of external stimuli (8). In other cell systems, the cytoskeleton apparently amplifies 3′ PI gradients in cells undergoing chemotaxis (25–27). These observations indicate that there is an intrinsic spatial bias, at the level of 3′ PI signaling, associated with cell morphological polarity and leading edge dynamics. Indeed, it has been suggested that positive feedback loops, involving PI 3-kinase, Rac/Cdc42, and/or the leading edge cytoskeleton, can give rise to spontaneous polarization (28–32).

In this article, we address the effects of cell morphology and morphological polarity on the 3′ PI pattern observed in PDGF-stimulated fibroblasts and shed light on the mechanisms that give rise to hot and cold spots. First, we describe improvements to our previous analytical approach that allow the numerical solution of model equations in cell contact area morphologies imported from image analysis software. This led to refined estimates of the model parameters, in particular the relative rates of 3′ PI turnover and diffusion. Second, in characterizing the hot and cold spots observed in TIRF experiments, we report that our cells typically exhibit multiple hot spots, associated with leading edge structures, whereas cold spots are less prevalent and found at the rear of the contact area. Although morphological polarity thus influences the 3′ PI pattern, we found that the local morphology of the contact area alone does not explain the presence of hot or cold spots, suggesting that these regions reflect local differences in 3′ PI production and/or turnover kinetics. Finally, we present an analysis of the 3′ PI accumulation and decay kinetics in hot spots. We find that their apparent kinetics are consistent with a combination of enhanced PI 3-kinase activation, regulation of 3′ PI turnover, and/or slow or constrained 3′ PI diffusion, suggesting mechanisms by which local 3′ PI levels are governed in leading edge structures.

MATERIALS AND METHODS

cDNA constructs, cell culture, and transfection

The GFP-AktPH construct consists of the specific 3′ PI-binding, pleckstrin homology domain of mouse Akt1 attached with a short linker to the C-terminus of enhanced green fluorescent protein (EGFP), made by cloning into BamHI/XbaI of pEGFP-C1 (Clontech, Palo Alto, CA). This insert was also cloned into the same sites of pEYFP-C1 and pECFP-C1 to produce yellow- and cyan-emitting probes, respectively. Membrane-targeted Lyn-CFP contains the palmitoylation sequence from Lyn (33) cloned into pECFP-N1. NIH 3T3 fibroblasts (American Type Culture Collection, Manassas, VA) were subcultured in 10-cm tissue culture dishes using Dulbecco's modified Eagle's medium with 10% fetal bovine serum, 2 mM L-glutamine, and the antibiotics penicillin and streptomycin as the growth medium. Unless otherwise noted, all tissue culture reagents were from Invitrogen (Carlsbad, CA). Cells were seeded in growth medium onto 25-mm square glass coverslips, precoated with poly-D-lysine, and later transfected with 1–2 μg of the vector(s) indicated using Lipofectamine Plus (Invitrogen). After 24 h, transfected cells were incubated in serum-free Dulbecco's modified Eagle's medium with 2 mM L-glutamine, the antibiotics penicillin and streptomycin, and 1 mg/ml fatty acid-free bovine serum albumin (Sigma, St. Louis, MO) for 3–5 h before imaging.

Total internal reflection fluorescence microscopy

Total internal reflection fluorescence (TIRF) microscopy is a mode of live-cell imaging whereby fluorophores in close proximity to the cell-substratum contact area are selectively excited by an evanescent wave, which penetrates a characteristic distance of ~100 nm into the cell (34–36). Our prism-based TIRF microscope was described in detail previously (22). Briefly, two laser heads from Melles-Griot (Irvine, CA) were used: a tunable wavelength Ar ion laser head, emitting lines of 488 nm (EGFP, 60 mW) or 514 nm (EYFP, 60 mW), and a HeCd laser head, emitting a 442-nm line (ECFP, 120 mW). All lines were used at maximum power, and the measured incidence angle of the reflected beam ranged from 68 to 69° across experiments. Band-pass emission filters (Chroma, Rockingham, VT) were 480/30 nm for ECFP, 515/30 nm for EGFP, and 535/30 nm for EYFP. Digital images were acquired using an ORCA ER-cooled CCD (Hamamatsu, Bridgewater, NJ) and Metamorph software (Universal Imaging, West Chester, PA). The imaging buffer was composed of 20 mM HEPES pH 7.4, 125 mM NaCl, 5 mM KCl, 1.5 mM $MgCl_2$, 1.5 mM $CaCl_2$, 10 mM glucose, and 2 mg/ml fatty acid-free bovine serum albumin. Fields of cells were visualized at a combined magnification of 25× or 12.5×, and TIRF images were acquired with 2×2 binning every 10–20 s over a 20–30-min time course. The exposure time × gain setting was fixed at ~400 ms for EGFP and EYFP constructs and ~2400 ms for ECFP constructs.

Association-dissociation experiments and analysis of fluorescence profiles in cell contact area geometries

In *association-dissociation* experiments, cells transfected with GFP-AktPH or its spectral variants are stimulated with a maximal dose of PDGF-BB (Peprotech, Rocky Hill, NJ) for ~10 min, during which an increase in TIRF fluorescence is observed (association). Thereafter, a high concentration of wortmannin (Sigma) or LY294002 (Calbiochem, San Diego, CA) is added to rapidly block the PI 3-kinase activity, isolating the degradation of 3′ PI lipids (dissociation). Experiments and image processing were performed as described previously (22).

The normalized fluorescence data from such experiments can be directly compared with a mathematical model that accounts for 3′ PI insertion, diffusion, and turnover in the adherent (i.e., bottom) and nonadherent (i.e., top) portions of the plasma membrane, as well as the binding of the GFP-AktPH probe (see the Appendix). In our previous analytical approach (21), the dimensionless model parameters Da, σ, p_{ss}, and x_0 were estimated directly from four fluorescence metrics: the initial fluorescence (f_0), the extent of the dip in fluorescence in the center of the contact area (f_{min}), the steady-state fluorescence value at the center ($f_{ss}(0)$), and the average fluorescence value at steady state ($\bar{f}_{ss}$). This procedure was previously carried out for six limiting cases of the model that considered the extremes of lipid-probe interaction parameters and top-bottom polarity of 3′ PI insertion; the model calculations, assuming a hemispherical cell, were finally fit to the real-time data using two additional parameters: a lag time, t_{lag}, and the degradation rate constant, k (21).

In this work, a two-step approach was adopted. We first assumed a flat, two-sided disk (pancake) morphology for the model cell, for which a closed-form analytical solution was derived (see the Appendix). The dimensionless parameters (Da, σ, p_{ss}, x_0) determined for the disk model served as initial guesses for the second step, in which model calculations were performed

using the actual contact area geometry of each cell. To achieve this, the outline of each cell was imported from a thresholded image into the finite-element modeling package, FEMLAB (Comsol, Burlington, MA). As in the disk model, the nonadherent plasma membrane was assumed to be flat, with the same shape as the contact area, and the 3′ PI concentrations and fluxes were matched at all corresponding points along the peripheries of the two domains in FEMLAB. The two-sided disk model was used to confirm the accuracy of the finite-element calculations. It was also confirmed that the mesh, automatically generated by FEMLAB, was sufficiently refined. Model calculations were used to generate stacks of simulated images for sequential association and dissociation kinetics. Identical line scans were taken from both the model and experimental stacks and directly compared; an interpolation macro was written in MATLAB (MathWorks, Natick, MA) to estimate the normalized fluorescence values at the same pixel locations as in the experimental line scan. Finally, the values of Da, σ, and x_0 were adjusted in an iterative fashion to match the initial and steady-state fluorescence profiles observed in the association phase of the experiment.

Modeling of hot and cold spot regions

Hot and cold spots were modeled in FEMLAB as small regions at the periphery of the cell (mirrored in both the top and bottom domains) with different properties from the rest of the membrane. The governing equations were solved in dimensionless form, and so the parameter values in these regions are defined relative to their corresponding values in the bulk membrane. To be consistent with experimental observations, only the bottom domain of the cell contributes to the average fluorescence value reported for the hot/cold spot.

RESULTS

Contact area morphology affects the radial pattern of 3′ PI lipids in response to PDGF

To assess the effect of cell shape on the calculated 3′ PI and fluorescence profiles in our model, we developed protocols for performing finite-element calculations with contact area geometries imported from image analysis software (Fig. 1). In the previous model, the plasma membrane was approximated as the surface of a hemisphere, with matching boundary conditions at the circular interface joining the adherent and nonadherent membrane domains (21). Another ideal geometry, perhaps more applicable to thinly spread fibroblasts, is the two-sided disk (Fig. 1 *a*). For a circular contact area, these represent two extremes, with the nonadherent membrane comprising two-thirds and one-half of the total membrane area, respectively. It was postulated, and later confirmed, that this difference does not affect the quality of fit to experimental fluorescence profiles or the estimated values of the two main parameters of interest, the 3′ PI diffusion coefficient D and turnover rate constant k (results not shown). Our current model, like the two-sided disk, assumes that the cell is flat but uses the true shape of each cell's contact area (Fig. 1 *a*).

The same cohort of cells analyzed previously (22), for which fluorescence data were already processed, were reanalyzed using the two-sided disk model and the true contact area protocol. For simplicity, the most broadly applicable limiting case (case *1*, with 3′ PIs in excess and no 3′ PI production in the contact area) was assumed in all calculations. Thus, 33 out of 36 cells yielded dimensionless parameters from both models. A representative comparison of measured and calculated responses to uniform PDGF

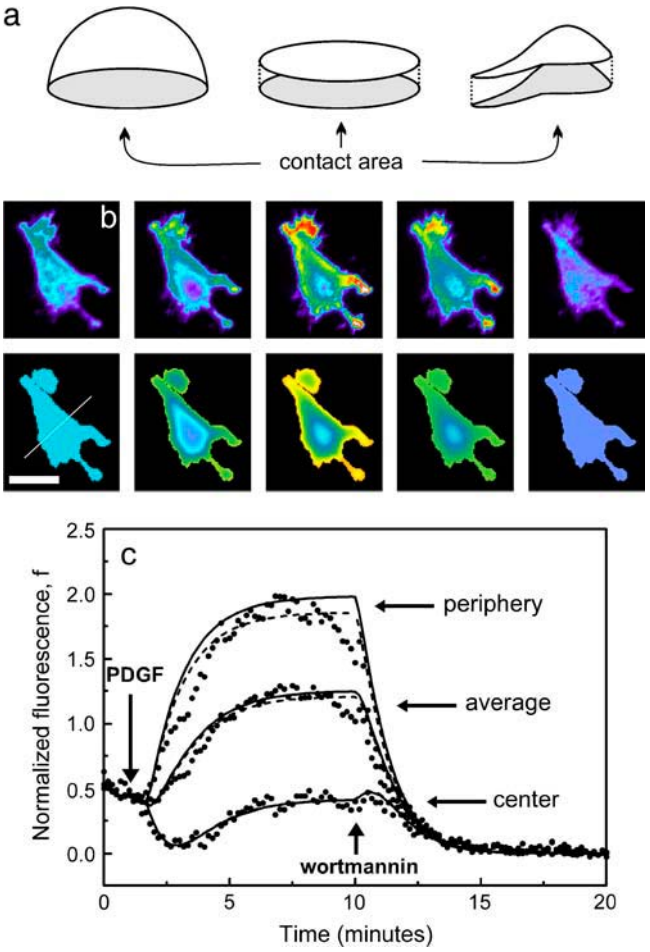

FIGURE 1 Calculated 3′ PI lipid profiles in response to PDGF stimulation using true contact area geometries. (*a*) Cell geometries considered in our past and present models. From left to right: hemisphere; two-sided disk; true contact area. (*b*) The top row of the montage shows TIRF images of a representative GFP-AktPH-transfected fibroblast in an association-dissociation experiment, whereas the bottom row shows virtual images assembled from corresponding finite-element modeling calculations. The images were taken, from left to right: before stimulation; 2 min after PDGF addition; 7 min after PDGF addition (steady state); 0.5 min after subsequent PI 3-kinase inhibition (5 μM wortmannin); and 10 min after inhibition (cytosolic fluorescence only). The line in the bottom left panel indicates the fluorescence profile used for model fitting. Scale bar = 20 μm. (*c*) Fit of the two-sided disk model (*dashed curves*) and true contact area model (*solid curves*) for the cell depicted in *b*. Dimensionless model parameters Da, σ, x_0, and p_{ss} were estimated for the disk model (7.30, 19.3, 0.0668, and 0.270, respectively) from four fluorescence metrics associated with the center and average fluorescence, taken from the line scan as described under Materials and Methods. Based on previous experience, it was assumed that 3′ PI is in excess ($\mu = 5$) and that PI 3-kinase is completely recruited to the top of the cell ($\nu = 0$). Da, σ, and x_0 were adjusted to give adequate agreement for the true contact area model ($Da = 6.25, \sigma = 21.5, x_0 = 0.0591$). For illustrative purposes, the fit to the entire time course is shown, with a 3′ PI turnover rate constant of $k = 0.72$ min^{-1} in the association phase and a lag time of $t_{lag} = 40$ s.

stimulation, followed by PI 3-kinase inhibition (association-dissociation experiment), is shown in Fig. 1 *b* and Movie *S*1 (Supplementary Material). The two models give comparable fits to the fluorescence profile taken through the center of the contact area, once the dimensionless parameters are adjusted for the true contact area model (Fig. 1 *c*). From these adjustments, we infer the effect of contact area geometry on the parameter estimation.

Of particular interest is the value of the Damköhler number,

$$Da = kL^2/D, \tag{1}$$

where L is the half-width of the contact area where the measured line scan was taken; its value characterizes the spatial range of locally produced 3′ PIs (Fig. 2). When a cell is elongated, the value of Da required to achieve a given gradient depth across the width (short axis) of the cell is lower than that of a circular cell. As expected then, the true contact area model nearly always yielded a lower estimate of Da than the two-sided disk (Fig. 2 *a*), with greater differences at lower Da (shallow gradients). The span of Da values among cells is largely attributed to variation in cell width. The spatial range, defined as the mean distance traveled by 3′ PIs during their lifetime,

$$\text{Range}\ (\mu\text{m}) = (4D/k)^{1/2}, \tag{2}$$

varied among cells but over a smaller relative span (Fig. 2 *b*), with a mean ± SD of 12.0 ± 3.7 μm for the true contact area geometry compared with 9.2 ± 3.0 μm for the disk model.

Curious to see if the change in the Da estimation could be predicted using a metric that describes the shape of the cell, we adapted the analysis commonly used for estimating diffusion resistance in the rate of reaction observed in porous catalyst particles. For particles of arbitrary shape, the reduction in observed rate is approximately defined by a single parameter, the Thiele modulus $\phi = (V_p/A_p)(k/D)^{1/2}$, where V_p and A_p are the volume and surface area of the particle, respectively (37). In two dimensions, we substitute V_p/A_p with the area/perimeter ratio, which is $R/2$ for a disk. Hence, the Da value estimated from the disk model was adjusted by replacing L with 2× the actual area/perimeter ratio of each contact area, determined from a hand-traced outline of the cell body (excluding thin protrusions). This approach was successful in approximating the Da found using the true contact area (Fig. 2 *c*). Consequently, the shape of the cell affects the 3′ PI lipid profile, but to a certain degree this change can be predicted using a simple geometric analysis.

Hot and cold spots of 3′ PI signaling

From the association-dissociation experiments it was apparent that certain contact area regions are significantly more or less fluorescent (by approximately a factor of 2) than neighboring regions. These localized regions of high and low

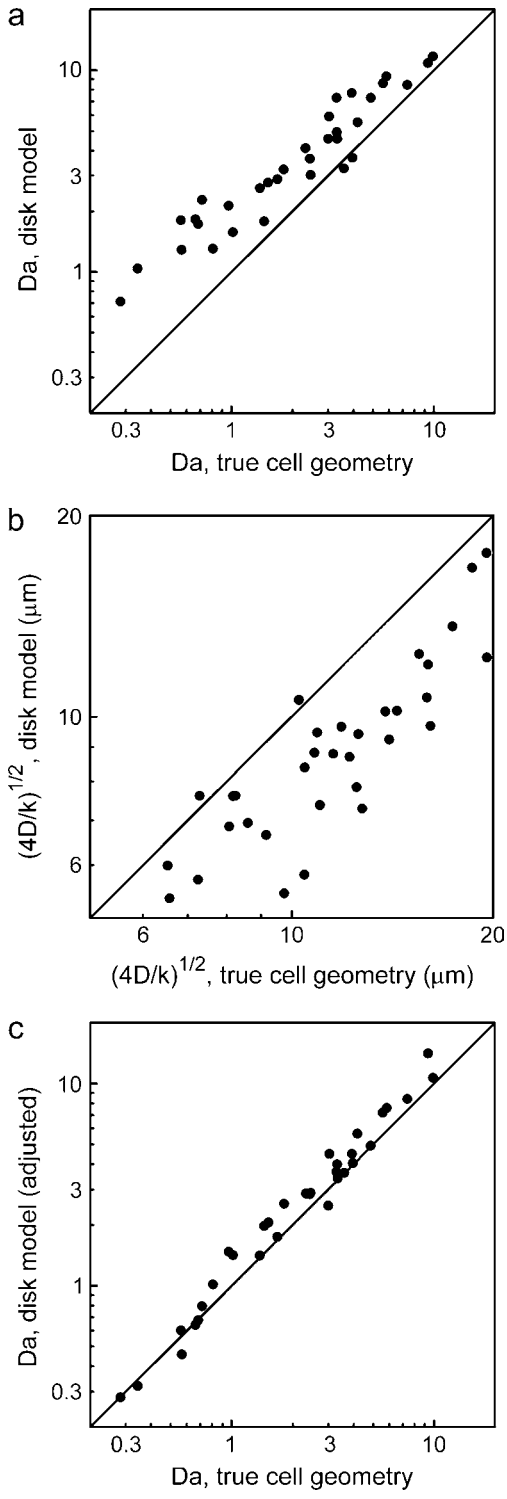

FIGURE 2 The assumed geometry of the contact area affects the estimation of Da, which compares the rates of 3′ PI turnover and diffusion. (*a*) Estimated values of Da (Eq. 1), from fits to the two-sided disk and true contact area models, are correlated for 33 cells. (*b*) The corresponding correlation of the estimated spatial ranges (Eq. 2) from the two models is also shown. (*c*) The Da values estimated using the disk model may be adjusted, using 2 × area/perimeter as the relevant length scale, to closely approximate the true contact area model estimate. In each plot, the solid line is $y = x$.

fluorescence, identified by inspection of TIRF images, are termed hot and cold spots, respectively. In all cases, these differences in fluorescence disappeared by the end of the dissociation phase (after PI 3-kinase inhibition). In control experiments with cells expressing soluble ECFP/EYFP or membrane-targeted lyn-CFP, regions with higher or lower fluorescence were seen much less frequently and differed in intensity by ~25% or less; the same trends were observed in cells co-transfected with YFP-AktPH/lyn-CFP, YFP-AktPH/ECFP, or CFP-AktPH/EYFP, in which there were no correlations between the two fluorescence channels (data not shown). We conclude that regions of significantly higher or lower GFP-AktPH fluorescence report local differences in the density of 3′ PI lipids.

A total of 49 cells transfected with GFP-AktPH were analyzed and found to contain a total of 129 hot spots and 39 cold spots. Fig. 3 *a*, a histogram of the number of hot and cold spots per cell, illustrates that hot spots were much more abundant than cold spots. The vast majority of the cells exhibited at least two hot spots and either zero or one cold spot.

Hot spots were generally found around the periphery of the cell (92%) and specifically in areas such as the tips of protruding structures and at leading edges. Nearly half (47%) of the hot spots exhibited noticeably higher-than-average intensity before the addition of PDGF, and nearly all (97%) maintained a higher fluorescence throughout the PDGF stimulation. Although cold spots were also found around the periphery, there were two distinct types. Most (59%) persisted throughout PDGF stimulation and occurred at the tips of extensions that might be trailing uropodia; these cold spots typically showed minimal response to PDGF during the association-dissociation protocol, but only 17% ($n = 4$) of them were noticeably cold before stimulation. In the other population (41%), the cold spots were not cold initially or at steady state, but lagged behind the rest of the cell for a certain period after PDGF addition; we refer to this population as transient cold spots.

Given the effect of contact area morphology on the calculated 3′ PI pattern (Fig. 1) and the prevalence of hot and cold spots in membrane extensions, we asked whether or not cell shape could explain the presence of apparent hot or cold spots. This possibility was ruled out through a simple analysis. As proven in the Appendix, the uniform stimulation model predicts the same 3′ PI level at all points along the cell periphery, regardless of contact area shape. Consequently, higher fluorescence in a thin extension cannot be attributed to geometric effects. Curvature of the nonadherent membrane also cannot explain significant differences in 3′ PI level; at steady state, the maximum difference between periphery 3′ PI levels in the disk and hemisphere models is ≈30% (one-half versus two-thirds); if anything, this would yield slightly lower fluorescence intensities in flat extensions compared to the periphery of the cell body. To illustrate this conclusion, TIRF images and finite-element calculations

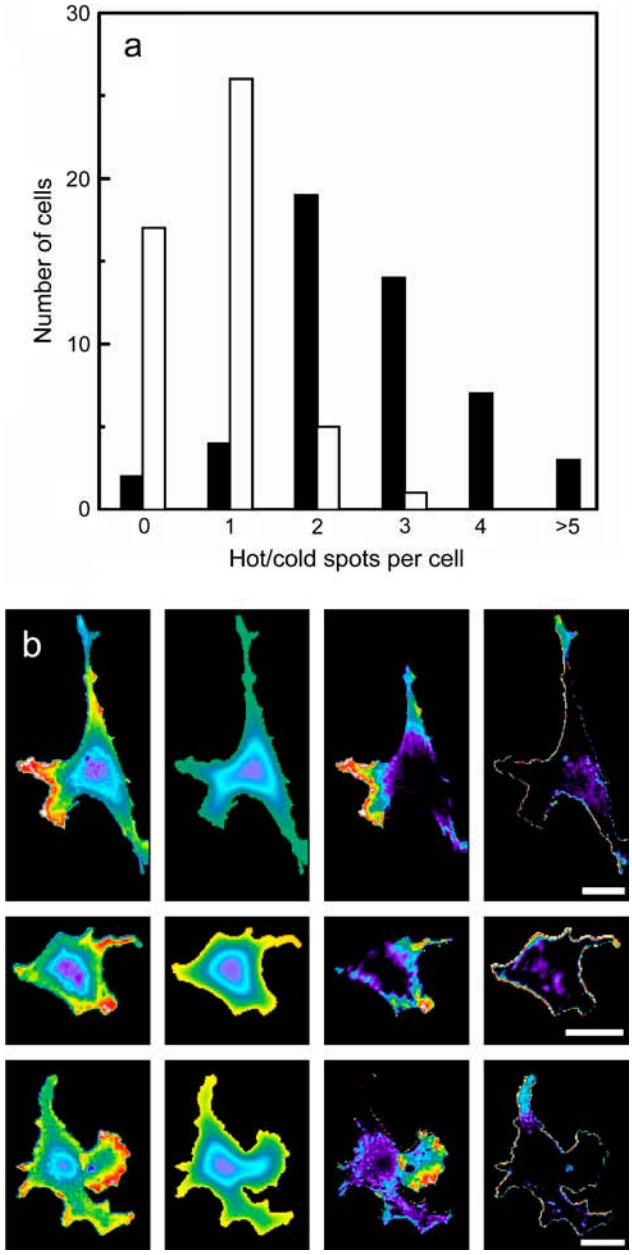

FIGURE 3 Hot and cold spots of 3′ PI signaling. Hot/cold spots are defined as localized regions in the contact area of a GFP-AktPH-transfected cell with noticeably higher/lower fluorescence than adjacent regions. (*a*) Histogram of the number of hot (*solid bars*) and cold (*open bars*) spots per cell, recorded for 49 cells. (*b*) Contact area morphology alone cannot account for hot or cold spots. Each row of the montage depicts the steady-state response to PDGF stimulation of a different representative cell. The first column shows the TIRF image, averaged over the time interval used to calculate the steady-state metrics, and the second column shows the virtual image obtained from model calculations as described under Fig. 1; these images use the same pseudo-color scale. The third column is the result of subtracting the virtual image from the TIRF image, and the fourth column is the result of subtracting the TIRF image from the virtual image. Scale bars are 20 μm.

were compared after maximal PDGF stimulation (Fig. 3 *b*). Subtracting the steady-state model prediction from the TIRF image or vice versa, it is clear that hot and cold spots identified from TIRF images have significantly higher or lower fluorescence intensities, respectively, than those predicted by the uniform stimulation model. We conclude that hot and cold spots arise from local differences in 3′ PI production, turnover, and/or diffusion.

Hot and cold spots exhibit distinct kinetics in association-dissociation experiments

The kinetics of the hot and cold spot responses to the association-dissociation protocol were also characterized (Fig. 4). A predominant characteristic of hot spots in this regard was a sluggish response compared with the rest of the cell (Fig. 4, *a* and *c*, and Movie *S*2 in the Supplementary Material). Specifically, in the association phase of the experiment, such a hot spot exhibits a slower approach to the steady state; its fluorescence intensity continues to increase after the fluorescence profile in the cell body has apparently settled upon a pseudo-steady state. Further, during the dissociation phase, whereas the fluorescence profile in the cell body rapidly becomes homogeneous as it decays (22), the fluorescence intensity of the hot spot fails to converge with that of the cell body until all of the 3′ PI is consumed (Fig. 4, *a* and *c*).

Cold spots came in two varieties, persistent and transient, as noted in the previous section. Whereas persistent cold spots tended to show very little response and thus no discernable kinetic signature, a representative example of the kinetics seen in the transient cold spot population is shown in Fig. 4, *b* and *d*, and Movie *S*3 (Supplementary Material). Initially, such cold spots appear no less bright than other peripheral regions of the cell body (excluding the obvious hot spots), but shortly after PDGF addition the cold spot is much dimmer than other peripheral areas and in fact dimmer than it was initially (Fig. 4 *b*). The fluorescence eventually merges with the rest of the cell body at steady state, and in the dissociation phase these regions do not differ from neighboring regions (Fig. 4 *d*). Taken together, we conclude that the kinetic features of certain hot and cold spot responses are different and thus reflect different mechanisms.

Motivated by the prevalence of hot spots in our cells and their unique kinetic features in both phases of the experiment, hot spot responses were further characterized through the following quantitative analysis (Fig. 5). For each cell, a region at the periphery of the cell body was chosen as a reference. Its decay in normalized fluorescence during the dissociation phase was fit to an appropriate function (which

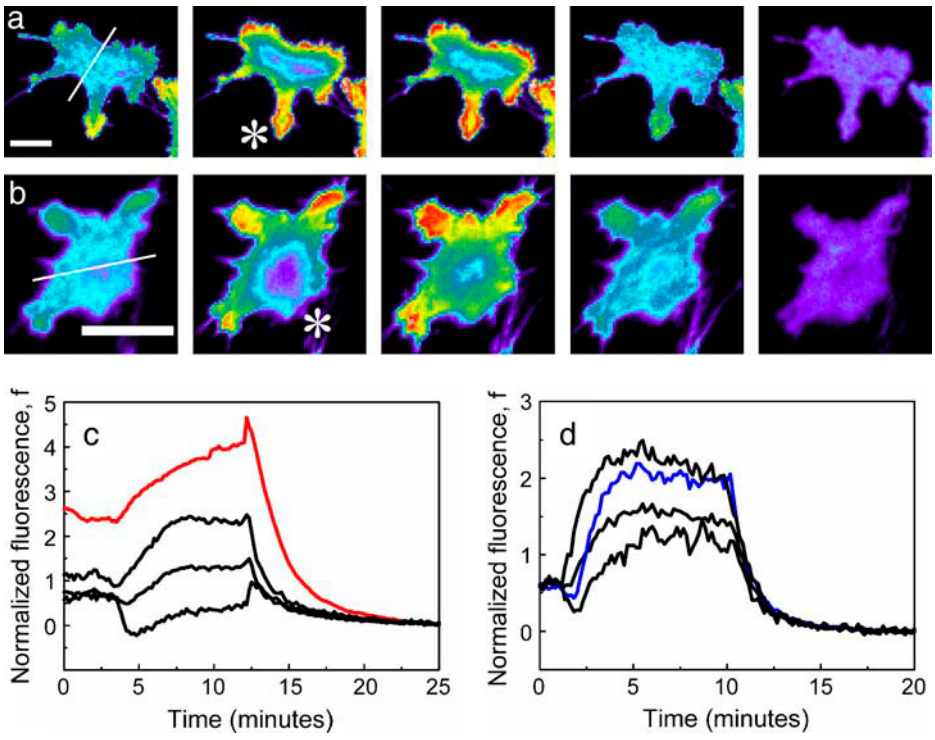

FIGURE 4 Characteristic response kinetics of hot and transient cold spots. TIRF images and time courses of representative hot (*a* and *c*) and cold (*b* and *d*) spots (denoted by the asterisks in *a* and *b*) in association-dissociation experiments. (*a*) The images were taken, from left to right: before PDGF addition; after PDGF stimulation, with the cell body at pseudo-steady state but the hot spot still increasing in intensity; at steady-state; after wortmannin addition, with the cell body more or less uniform but the hot spot decay lagging; and after complete fluorescence decay. Scale bar = 20 μm. (*b*) The images were taken, from left to right: before PDGF addition; after stimulation, when the cold spot is apparent; at steady state; after wortmannin addition, with the cold spot and the rest of the cell body uniform; and after complete fluorescence decay. Scale bar = 20 μm. (*c*) Hot spot kinetics. The center, average, and periphery fluorescence, associated with the line scan in *a*, are shown as a function of time (*black curves*) as in Fig. 1, along with the fluorescence time course of the hot spot (*red curve*). (*d*) Transient cold spot kinetics. The center, average, and periphery fluorescence, associated with the line scan in *b*, are shown as a function of time (*black curves*) as in Fig. 1, along with the fluorescence time course of the cold spot (*blue curve*).

assumes exponential decay of 3′ PI concentration and pseudo-equilibrium with the GFP-AktPH probe),

$$f(t) = \frac{d_1 \exp(-t/d_2)}{1 + d_3 \exp(-t/d_2)}, \quad (3)$$

to estimate the time $t_{1/2}$ at which the fluorescence had fallen to half of its initial value (in terms of the decay fit parameters, $t_{1/2} = d_2 \ln(2 + d_3)$). At this time, the normalized fluorescence values and rates of fluorescence decay for the reference region and all peripheral hot spots in that cell were estimated by linear regression over a 1-min interval. The *value ratio* is defined as the normalized fluorescence of a particular hot spot divided by that of the reference region. A value ratio >1 indicates that the hot spot fluorescence had not yet merged with that of the cell body at $t_{1/2}$. The *decay ratio* is defined as the specific rate of decay (−slope/value) of the hot spot divided by that of the reference region. A decay ratio ≤1, together with a value ratio >1, indicates that the hot spot and reference fluorescence intensities have neither converged nor are in the process of doing so. Based on these criteria, with a reasonable value ratio cutoff of 1.2, 61% of the hot spots failed to converge with the reference region (Fig. 5). Further, 48% of these hot spots (or 29% total) decayed at a significantly slower relative rate (decay ratio <0.8) than the reference region; this observation will be significant in our subsequent modeling analysis.

The response during the association phase was quantitatively assessed by fitting hot spot and reference region kinetics to single exponentials ($f - f_0 = a_1[1 - \exp(-t/a_2)]$, with t adjusted for the apparent lag time after PDGF addition). Fifty-eight percent of the peripheral hot spots showed slower kinetics in the association phase, as judged by a time constant a_2 at least 20% higher than the corresponding reference region, and the hot spots that showed slower decay ratios in the dissociation phase were much more likely to satisfy this criterion (Fig. 5).

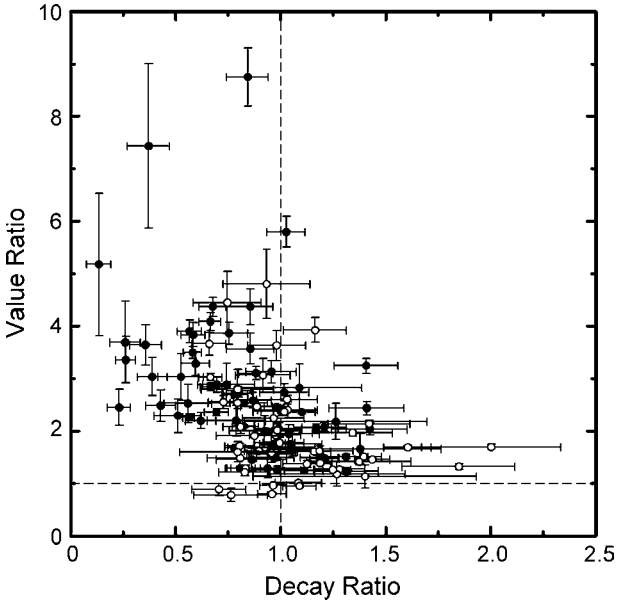

FIGURE 5 Quantitative analysis of hot spot kinetics. This plot shows quantitative metrics that characterize the fluorescence decay during the dissociation phase in each of the periphery hot spots analyzed ($n = 119$). In each cell, a reference region at the periphery of the cell body contact area (not a hot or cold spot) was chosen, and the time at which its fluorescence had decayed by 50% ($t_{1/2}$) was estimated (Eq. 3). At this time, the normalized fluorescence value and rate of decay for the reference region and all hot spots in that cell were estimated by linear regression over a 1-min interval spanning the $t_{1/2}$ (seven time points, with the midpoint time being the closest to $t_{1/2}$). A hot spot's value ratio is defined as its fluorescence at the $t_{1/2}$ divided by that of the reference region, whereas its decay ratio is defined as the specific rate of decay (−slope/value) of the hot spot divided by that of the reference region. A decay ratio ≤1, together with a value ratio >1, indicates that the hot spot and reference fluorescence intensities have neither converged nor are in the process of doing so. The error bars were determined by propagation of standard errors. The closed circles indicate hot spots that displayed at least a 20% slower (higher) time constant in the association phase, whereas the open circles indicate hot spots that did not meet this criterion.

Hot spot responses are consistent with a combination of mechanisms: enhanced PI 3-kinase activation, reduced 3′ PI turnover, and/or slow or constrained 3′ PI diffusion

Given that hot spots arise from local differences in 3′ PI production, turnover, and/or diffusion, we sought to elucidate which of these mechanisms are at play. Hot spots consistently showed distinct kinetics in both phases of the experiment, which is significant because differences found during the dissociation phase can only be attributed to differing rates of 3′ PI turnover and/or diffusion. When the turnover rate constant k and diffusion coefficient D are the same throughout the plasma membrane, the 3′ PI density at all points along the contact area periphery decays according to a single exponential (see the Appendix):

$$x(t) = x(0)e^{-kt}. \quad (4)$$

The 3′ PI density at the center of the contact area apparently decays more slowly because of the net diffusion of lipid from the periphery, until the 3′ PI profile in the cell body converges as described in the previous section. Likewise, a region with higher local 3′ PI density initially would tend to decay faster as the profile converges. One concludes that the sluggish dissociation responses exhibited by most hot spots reflect a non-homogeneous k and/or D.

We proceeded to model hot spots simply as defined subcompartments of the membrane with their own values of the model parameters, and analysis of the model led to a number of conclusions (Fig. 6). First, in hot spots with enhanced PI 3-kinase activity alone (Fig. 6, *a* and *d*), we expect that the fluorescence intensity would rapidly merge with that of the cell body during the dissociation phase; this is illustrated in Fig. 6 *d*. Second, if enhanced PI 3-kinase activity is coupled with very slow or constrained diffusion in the hot spot, (Fig. 6, *b* and *e*), its 3′ PI density is effectively

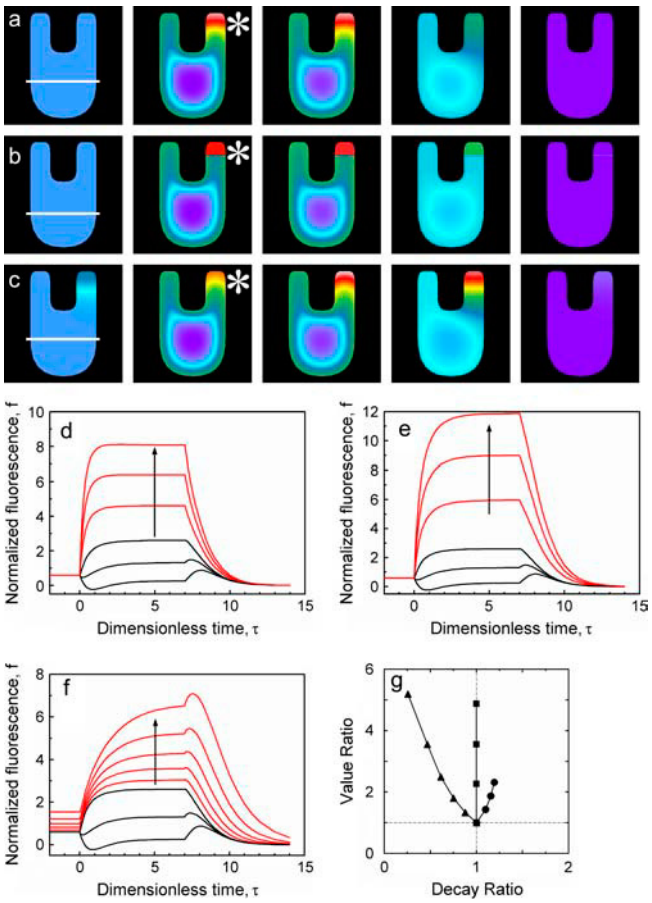

FIGURE 6 Analysis of mechanisms that give rise to hot spots. (*a–c*) The images depict model calculations of a hypothetical association-dissociation experiment and correspond to roughly the same times depicted in Fig. 4 *a*, with $\tau = kt = 0, 2, 7$ (just before PI 3-kinase inhibition), 8, and 14 from left to right. Model parameters in the cell body are $Da = 6, \sigma = 10, x_0 = 0.05, \nu = 0, \kappa = 2$, and $\mu = 5$. For simplicity, a single hot spot with different kinetic properties was placed at the tip of the right pseudopod (in both the contact area and nonadherent membrane), representing ~4% of the total membrane area (*asterisk*). In *a*, the hot spot has enhanced PI 3-kinase activation ($\upsilon_b = \upsilon_t = 1.5$). The hot spot in *b* has enhanced PI 3-kinase activation ($\upsilon_b = \upsilon_t = 1$) and no 3′ PI flux between the hot spot and the rest of the membrane (constrained diffusion). In *c*, the 3′ PI turnover rate in the hot spot was reduced to zero, but otherwise the region is normal. (*d–f*) The center, average, and periphery fluorescence for the line scans in *a–c* are shown as a function of time (*black curves*), along with the hot spot fluorescence assuming different parameters (*red curves*). In *d* and *e*, the hot spot has different 3′ PI insertion rates relative to the top of the cell body (1, 1.5, and 2 in the direction of the *arrows*); in *e*, the hot spot is also subject to constrained diffusion as in *b*. In *f*, the hot spot has a different 3′ PI turnover rate constant relative to the cell body (0.8, 0.6, 0.4, 0.2, and 0 in the direction of the *arrow*). (*g*) The hot spots depicted in *d* (enhanced PI 3-kinase, *circles*), *e* (enhanced PI 3-kinase with constrained diffusion, *squares*), and *f* (slow turnover, *triangles*) were subjected to the same analysis as in Fig. 5 for comparison.

isolated from the rest of the membrane and thus decays according to Eq. 4 during the dissociation phase, at the same relative rate as the rest of the periphery. Thus, in this case the hot spot 3′ PI density does not converge with that of the cell body (Fig. 6 *e*). Finally, the 3′ PI density also fails to converge in hot spots with normal PI 3-kinase activation and 3′ PI diffusion but reduced 3′ PI turnover (Fig. 6, *c* and *f*, and Movie *S*4 in the Supplementary Material). Such hot spots would also tend to exhibit a higher local 3′ PI density before stimulation and a slower approach to the steady state during the association phase, consistent with the characteristics of a significant fraction of hot spots (Fig. 6 *f*). Of course, these effects would also arise if one assumes local differences in basal PI 3-kinase activity and the kinetics of receptor-stimulated PI 3-kinase activation.

To illustrate the effects of various mechanisms on the quantitative characteristics of fluorescence decay during the dissociation phase, we subjected the model kinetics shown in Fig. 6, *d–f*, to the same analysis used in Fig. 5 to characterize the experimentally observed kinetics (Fig. 6 *g*). The hot spots with enhanced PI 3-kinase alone have value and decay ratios that are both >1 by a modest amount, indicative of merging fluorescence values. Either slow/constrained diffusion or reduced turnover is required to produce hot spot decay that fails to merge with the cell body during the dissociation phase (value ratio >1 and decay ratio ≤ 1), but a key difference is that these two mechanisms tend to give different relative rates of decay. Slow or constrained diffusion keeps the value ratio high and brings the decay ratio very close to one; as outlined above, the 3′ PI level in a hot spot with slow/constrained diffusion and normal turnover decays at the same relative rate (% decrease per unit time) as regions at the periphery of the cell body. Reduced turnover produces a decay ratio <1 and is unique in this respect (Fig. 6 *g*).

In Fig. 5, we noted that a significant fraction of hot spots exhibited value ratios >1.2 and decay ratios <0.8, an indication of significant reduction in turnover. The fact that these hot spots also showed sluggish association kinetics is consistent with this view. From the spectrum of decay ratios observed, we conclude that hot spots arise from enhanced PI 3-kinase activation as well as reduced 3′ PI turnover, perhaps influenced by slow or constrained 3′ PI diffusion, although individual hot spots likely differ with respect to the dominant mechanism(s).

DISCUSSION

Numerous mathematical models have been developed and updated recently to describe eukaryotic spatial sensing phenomena (38,39), and quantitative data are being used to inform such models (27). Direct comparison of experiments and models is a critical step toward understanding the signaling mechanisms that govern gradient perception and other intracellular signaling systems (40). We now have a suitable modeling framework that describes uniform PDGF stimulation in fibroblasts, such that its extension to PDGF gradient sensing will be straightforward. By incorporating actual cell morphologies into this model, we have gained insights relevant to both the model implementation as well as the biology of the spatially regulated PI 3-kinase response.

We first employed this framework to more accurately estimate model parameters. Use of idealized, circular contact area geometry is adequate for estimating the spatial range of 3′ PIs (Eq. 2) within a factor of 2 or so, but it consistently underestimates this quantity. A good compromise for parameter estimation was found in the application of the Thiele modulus, commonly used to analyze diffusion-reaction coupling in heterogeneous catalysis. Although lateral 3′ PI diffusion is important for interactions between 3′ PI-bound proteins and other membrane-associated components, not to mention its potential role in smoothing out stochastic fluctuations, in this context it is detrimental to the maintenance of long-range 3′ PI gradients. As we now apply the finite-element modeling approach to characterize cells responding to PDGF gradients, in which cells vary with respect to their morphology and orientation relative to the PDGF source (I.C. Schneider and J.M. Haugh, unpublished), use of the true cell geometry and accurate parameter estimates are vital.

The second motivation for more realistic modeling of contact area geometry was to shed light on the mechanisms that give rise to localized regions with significantly higher or lower fluorescence intensity (hot and cold spots, respectively), observed in peripheral membrane structures that correlated strongly with the cell's morphological polarity. With geometric effects accounted for, we analyzed the hypothetical influences of local differences in PI 3-kinase activation and 3′ PI turnover and compared these effects with the kinetics typically observed in response to PDGF. Hot spots, typically found in numerous regions coinciding with (possibly competing) leading edge structures, were characterized by slower kinetics, exemplified by a dramatic time shift in the fluorescence decay kinetics after PI 3-kinase inhibition. From a quantitative analysis of these kinetics together with model calculations, we concluded that one of the mechanisms contributing to the higher 3′ PI densities in hot spots is a local reduction in the rate of 3′ PI turnover. Therefore, although pathways and feedback loops affecting PI 3-kinase activity at the leading edge have received considerable attention, we must also consider the local regulation of PI 3-phosphatases or other 3′ PI consumption pathways.

A PI 3-phosphatase studied actively in recent years is phosphatase and tensin homolog deleted on chromosome 10 (PTEN). In *Dictyostelium discoideum*, PTEN is localized at the plasma membrane in a reciprocal fashion with respect to PI 3-kinase; i.e., it is membrane-associated before stimulation, dissociates transiently in response to uniform chemoattractant stimulation, and is persistently membrane-localized at the rear and sides during chemotaxis (27,41,42). The localization and activity of mammalian PTEN, however, are subject to additional regulatory mechanisms, as implicated by its different domain structure (43). It remains possible, then, that the membrane binding and/or activity of mammalian PTEN or other 3′ PI phosphatases may be altered in a highly localized fashion, although the signaling determinants involved are presently uncertain. In our cells, we established previously that 3′ PI turnover is not globally regulated in response to PDGF (22), yet such enzymes do appear to be less active in or excluded from certain leading edge locations.

Although hot spots are apparently affected by regulation of 3′ PI turnover, we found that enhanced PI 3-kinase activation was also required to explain the degree of 3′ PI enrichment in many hot spots. Locally restricted 3′ PI diffusion may also be important, as has been implicated in PI 3-kinase-dependent signaling processes driving phagocytosis (44). Incidentally, the less abundant cold spots apparently arise from a lack of PDGF-stimulated PI 3-kinase activation in these regions, or in the case of transient cold spots, a delay in the PI 3-kinase activation kinetics (analysis not shown). Together, these effects are consistent with the notion that leading and trailing edges of the membrane exhibit unique signaling activities and/or present different environments for signaling to take place there.

We have analyzed the apparent relationship between morphological polarity and 3′ PI signaling, in the context of both unstimulated and PDGF-stimulated fibroblasts. This relationship leads us to speculate that cell polarity yields an intrinsic bias for directed migration, at the level of the 3′ PI pattern, which would either reinforce or antagonize the external bias of a PDGF gradient oriented in a certain direction. This concept is consistent with a model put forward recently, which is based on the correlation of spontaneous 3′ PI pulses at the leading edge with cell turning behavior during random and directed cell migration (45). Obviously, we present here only a snapshot of signaling that occurs during cell movement, which must be integrated with the control of cell polarity, membrane protrusion, and cell adhesiveness.

APPENDIX

3′ PI distribution in a uniformly stimulated cell approximated as a flat, two-sided membrane with any shape

Let x_t and x_b be the 3′ PI density profiles in the top (nonadherent) and bottom (contact area) domains of the plasma membrane. As in our previous model (21), PI 3-kinase activation is characterized by different time-dependent source terms in the top and bottom domains (υ_t and υ_b, respectively); here we explicitly assume that the 3′ PI diffusion coefficient and turnover rate constant (D and k, respectively) are the same in both domains. In mathematical terms, the conservation equations to be solved are

$$\frac{\partial x_t}{\partial \tau} = Da^{-1}\nabla^2 x_t - x_t + \upsilon_t(\tau);$$
$$\frac{\partial x_b}{\partial \tau} = Da^{-1}\nabla^2 x_b - x_b + \upsilon_b(\tau);$$
$$\tau = kt; \quad Da = kL^2/D. \tag{5}$$

The characteristic length scale, L, relates the size of the model domain to actual lengths. It is assumed here that the cell is flat, i.e., the top and bottom

domains are mirror images of one another, with exchange at the periphery; for now we make no other restriction on the shape of the cell. Denoting S as the shared periphery of both domains, the matching boundary conditions must be satisfied on S:

$$x_t|_S = x_b|_S = x|_S; \tag{6}$$

$$n \cdot \nabla x_t|_S = -n \cdot \nabla x_b|_S, \tag{7}$$

where n is the unit vector normal to the boundary. Eq. 7 may be expressed as

$$n \cdot \nabla(x_t + x_b)|_S = 0. \tag{8}$$

The form of Eq. 5, along with Eq. 8, yields a major simplification: if the initial lipid profiles also satisfy Eq. 5, the sum of $x_t + x_b$ at any corresponding position in the two boundaries, defined as x_{Tot}, is a function of time only:

$$x_t + x_b = x_{Tot}(\tau) = e^{-\tau}\left[x_{Tot}(0) + \int_0^\tau \upsilon e^{\tau'} d\tau'\right];$$
$$\upsilon(\tau) = \upsilon_t + \upsilon_b. \tag{9}$$

Incorporating Eq. 6, we obtain a closed-form boundary condition, which can be used to solve Eq. 5 for the bottom domain:

$$x|_S = x_{Tot}(\tau)/2. \tag{10}$$

Therefore, when the underlying assumptions are valid, the 3′ PI density is the same at all points around the periphery.

Solution for a two-sided disk

We turn now to a circular bottom domain of radius R ($L = R$), with a specified concentration at the periphery. The general solution is given in terms of $z = x_b - x|_S$, as a function of radial position $\rho = r/R$ and dimensionless time:

$$z(\rho,\tau) = 2\sum_{n=1}^{\infty} \Theta_n e^{-\beta_n \tau}\left[\Phi_{n,0} - \frac{\int_0^\tau (\upsilon_t - \upsilon_b) e^{\beta_n \tau'} d\tau'}{2\zeta_n}\right];$$
$$\Theta_n(\rho) = J_0(\zeta_n \rho)/J_1(\zeta_n); \quad J_0(\zeta_n) = 0;$$
$$\Phi_{n,0} = \int_0^1 z(\rho,0)\Theta_n \rho d\rho;$$
$$\beta_n = 1 + \zeta_n^2/Da, \tag{11}$$

where J_m are Bessel functions of order m. For the association phase of an experiment, in which PI 3-kinase is rapidly activated by maximal receptor stimulation ($\upsilon_t = 1$; $\upsilon_b = \nu$) and the 3′ PI profile is assumed to be flat initially ($x_b(\rho,0) = x_0$, $z(\rho,0) = 0$),

$$x|_S(\tau) = x_0 e^{-\tau} + \left(\frac{1+\nu}{2}\right)(1 - e^{-\tau});$$
$$z(\rho,\tau) = -(1-\nu)\sum_{n=1}^{\infty} \frac{\Theta_n}{\zeta_n \beta_n}(1 - e^{-\beta_n \tau}). \tag{12}$$

At steady state, the lipid profile simplifies to

$$x_{b,ss}(\rho) = \nu + \frac{(1-\nu)}{2}\frac{I_0(Da^{1/2}\rho)}{I_0(Da^{1/2})}. \tag{13}$$

For the dissociation phase of the experiment, in which PI 3-kinase activity is instantaneously blocked ($\upsilon_t = \upsilon_b = 0$), it is noted that Eq. 13 serves as the initial condition, with $x_{b,ss}(\rho) + x_{t,ss}(\rho) = 1 + \nu$ at all ρ. Hence,

$$x|_S = \left(\frac{1+\nu}{2}\right)e^{-\tau};\ z(\rho,\tau) = -(1-\nu)\sum_{n=1}^{\infty} \frac{\Theta_n e^{-\beta_n \tau}}{\zeta_n \beta_n}. \tag{14}$$

The derivation of Eq. 14 is obtained using either of the following identities:

$$\int_0^1 \Theta_n^2 \rho d\rho = \frac{1}{2};$$
$$\int_0^1 \frac{I_0(Da^{1/2}\rho)}{I_0(Da^{1/2})}\Theta_n \rho d\rho = \frac{\zeta_n}{Da + \zeta_n^2} = \frac{\zeta_n}{Da\beta_n}. \tag{15}$$

Fluorescence profile

Given a 3′ PI profile x_b, the normalized fluorescence profile, f, was determined as derived previously (21); assuming pseudo-equilibrium for GFP-AktPH/3′ PI binding,

$$f = (\sigma x_b/x_{Tot} - 1)p; \quad \sigma = V_{cyt}/A_c d_{cell};$$
$$p(\tau) = \frac{1 + \kappa + \mu x_{Tot} - \left[(1 + \kappa + \mu x_{Tot})^2 - 4\mu x_{Tot}\right]^{1/2}}{2};$$
$$\kappa = K_D V_{cyt}/P_{Tot}; \quad \mu = A_c X^*/P_{Tot}, \tag{16}$$

where V_{cyt} is the volume of the cytosol, A_c is the contact area, d_{cell} is the mean penetration depth of the evanescent wave, K_D is the AktPH/3′ PI dissociation constant, P_{Tot} is the total number of GFP-AktPH molecules in the cell, and X^* is an arbitrary scaling constant for the 3′ PI density. The quantity x_{Tot} was specified in Eq. 9.

SUPPLEMENTARY MATERIAL

An online supplement to this article can be found by visiting BJ Online at http://www.biophysj.org.

This work was supported by grants from the Office of Naval Research (No. N00014-03-1-0594), the Whitaker Foundation (No. RG-01-0150), and the Cell Migration Consortium Modeling Initiative. Microscopy equipment was purchased using funds from an award to J.M.H. from the Henry & Camille Dreyfus Foundation.

REFERENCES

1. Seppä, H., G. Grotendorst, S. Seppä, E. Schiffmann, and G. R. Martin. 1982. Platelet-derived growth factor is chemotactic for fibroblasts. *J. Cell Biol.* 92:584–588.
2. Pierce, G. F., T. A. Mustoe, B. W. Altrock, T. F. Deuel, and A. Thomason. 1991. Role of platelet-derived growth factor in wound healing. *J. Cell. Biochem.* 45:319–326.
3. Claesson-Welsh, L. 1994. Platelet-derived growth factor receptor signals. *J. Biol. Chem.* 269:32023–32026.
4. Heldin, C.-H., and B. Westermark. 1999. Mechanism of action and in vivo role of platelet-derived growth factor. *Physiol. Rev.* 79:1283–1316.
5. Wennström, S., P. Hawkins, F. Cooke, K. Hara, K. Yonezawa, M. Kasuga, T. Jackson, L. Claesson-Welsh, and L. Stephens. 1994. Activation of phosphoinositide 3-kinase is required for PDGF-stimulated membrane ruffling. *Curr. Biol.* 4:385–393.
6. Wennström, S., A. Siegbahn, K. Yokote, A. Arvidsson, C.-H. Heldin, S. Mori, and L. Claesson-Welsh. 1994. Membrane ruffling and chemotaxis transduced by the PDGF β-receptor require the binding site for phosphatidylinositol 3′ kinase. *Oncogene.* 9:651–660.

7. Kundra, V., J. A. Escobedo, A. Kazlauskas, H. K. Kim, S. G. Rhee, L. T. Williams, and B. R. Zetter. 1994. Regulation of chemotaxis by the platelet-derived growth factor receptor-β. *Nature*. 367:474–476.
8. Haugh, J. M., F. Codazzi, M. Teruel, and T. Meyer. 2000. Spatial sensing in fibroblasts mediated by 3′ phosphoinositides. *J. Cell Biol.* 151:1269–1279.
9. Ridley, A. J. 2001. Rho proteins, PI 3-kinases, and monocyte/macrophage motility. *FEBS Lett.* 498:168–171.
10. Rameh, L. E., and L. C. Cantley. 1999. The role of phosphoinositide 3-kinase lipid products in cell function. *J. Biol. Chem.* 274:8347–8350.
11. Fruman, D. A., R. E. Meyers, and L. C. Cantley. 1998. Phosphoinositide kinases. *Annu. Rev. Biochem.* 67:481–507.
12. Vanhaesebroeck, B., S. J. Leevers, K. Ahmadi, J. Timms, R. Katso, P. C. Driscoll, R. Woscholski, P. J. Parker, and M. D. Waterfield. 2001. Synthesis and function of 3-phosphorylated inositol lipids. *Annu. Rev. Biochem.* 70:535–602.
13. Nobes, C. D., and A. Hall. 1999. Rho GTPases control polarity, protrusion, and adhesion during cell movement. *J. Cell Biol.* 144: 1235–1244.
14. Ridley, A. J., M. A. Schwartz, K. Burridge, R. A. Firtel, M. H. Ginsberg, G. Borisy, T. J. Parsons, and A. R. Horwitz. 2003. Cell migration: integrating signals from front to back. *Science*. 302:1704–1709.
15. Servant, G., O. D. Weiner, P. Herzmark, T. Balla, J. W. Sedat, and H. R. Bourne. 2000. Polarization of chemoattractant receptor signaling during neutrophil chemotaxis. *Science*. 287:1037–1040.
16. Parent, C. A., B. J. Blacklock, W. M. Froehlich, D. B. Murphy, and P. N. Devreotes. 1998. G-protein signaling events are activated at the leading edge of chemotactic cells. *Cell*. 95:81–91.
17. Parent, C. A., and P. N. Devreotes. 1999. A cell's sense of direction. *Science*. 284:765–770.
18. Weiner, O. D. 2002. Regulation of cell polarity during eukaryotic chemotaxis: the chemotactic compass. *Curr. Opin. Cell Biol.* 14:196–202.
19. Merlot, S., and R. A. Firtel. 2003. Leading the way: directional sensing through phosphatidylinositol 3-kinase and other signaling pathways. *J. Cell Sci.* 116:3471–3478.
20. Postma, M., and P. J. M. Van Haastert. 2001. A diffusion-translocation model for gradient sensing by chemotactic cells. *Biophys. J.* 81:1314–1323.
21. Haugh, J. M., and I. C. Schneider. 2004. Spatial analysis of 3′ phosphoinositide signaling in living fibroblasts. I. Uniform stimulation model and bounds on dimensionless groups. *Biophys. J.* 86:589–598.
22. Schneider, I. C., and J. M. Haugh. 2004. Spatial analysis of 3′ phosphoinositide signaling in living fibroblasts. II. Parameter estimates for individual cells from experiments. *Biophys. J.* 86:599–608.
23. Pollard, T. D., and G. G. Borisy. 2003. Cellular motility driven by assembly and disassembly of actin filaments. *Cell.* 112:453–465.
24. Etienne-Manneville, S. 2004. Cdc42—the centre of polarity. *J. Cell Sci.* 117:1291–1300.
25. Wang, F., P. Herzmark, O. D. Weiner, S. Srinivasan, G. Servant, and H. R. Bourne. 2002. Lipid products of PI_3Ks maintain persistent cell polarity and directed motility in neutrophils. *Nat. Cell Biol.* 4: 513–518.
26. Weiner, O. D., G. Servant, M. D. Welch, T. J. Mitchison, J. W. Sedat, and H. R. Bourne. 1999. Spatial control of actin polymerization during neutrophil chemotaxis. *Nat. Cell Biol.* 1:75–81.
27. Janetopoulos, C., L. Ma, P. N. Devreotes, and P. A. Iglesias. 2004. Chemoattractant-induced phosphatidylinositol 3,4,5-trisphosphate accumulation is spatially amplified and adapts, independent of the actin cytoskeleton. *Proc. Natl. Acad. Sci. USA.* 101:8951–8956.
28. Weiner, O. D., P. O. Neilsen, G. D. Prestwich, M. W. Kirschner, L. C. Cantley, and H. R. Bourne. 2002. A $PtdInsP_3$- and Rho GTPase-mediated positive feedback loop regulates neutrophil polarity. *Nat. Cell Biol.* 4:509–512.
29. Srinivasan, S., F. Wang, S. Glavas, A. Ott, F. Hofmann, K. Aktories, D. Kalman, and H. R. Bourne. 2003. Rac and Cdc42 play distinct roles in regulating $PI(3,4,5)P_3$ and polarity during neutrophil chemotaxis. *J. Cell Biol.* 160:375–385.
30. Wedlich-Soldner, R., S. Altschuler, L. Wu, and R. Li. 2003. Spontaneous cell polarization through actomyosin-based delivery of the Cdc42 GTPase. *Science*. 299:1231–1235.
31. Nalbant, P., L. Hodgson, V. Kraynov, A. Toutchkine, and K. M. Hahn. 2004. Activation of endogenous Cdc42 visualized in living cells. *Science*. 305:1615–1619.
32. Postma, M., J. Roelofs, J. Goedhart, H. M. Loovers, A. J. Visser, and P. J. M. Van Haastert. 2004. Sensitization of *Dictyostelium* chemotaxis by phosphoinositide-3-kinase-mediated self-organizing signalling patches. *J. Cell Sci.* 117:2925–2935.
33. Teruel, M. N., T. A. Blanpied, K. Shen, G. J. Augustine, and T. Meyer. 1999. A versatile microporation technique for the transfection of cultured CNS neurons. *J. Neurosci. Methods*. 93:37–48.
34. Axelrod, D. 2001. Total internal reflection fluorescence microscopy in cell biology. *Traffic*. 2:764–774.
35. Steyer, J. A., and W. Almers. 2001. A real-time view of life within 100 nm of the plasma membrane. *Nat. Rev. Mol. Cell Biol.* 2: 268–275.
36. Toomre, D., and D. J. Manstein. 2001. Lighting up the cell surface with evanescent wave microscopy. *Trends Cell Biol.* 11:298–303.
37. Aris, R. 1957. On shape factors for irregular particles. I. The steady-state problem. Diffusion and reaction. *Chem. Eng. Sci.* 6:262–268.
38. Subramanian, K. K., and A. Narang. 2004. A mechanistic model for eukaryotic gradient sensing: spontaneous and induced phosphoinositide polarization. *J. Theor. Biol.* 231:49–67.
39. Ma, L., C. Janetopoulos, L. Yang, P. N. Devreotes, and P. A. Iglesias. 2004. Two complementary, local excitation, global inhibition mechanisms acting in parallel can explain the chemoattractant-induced regulation of PI(3,4,5)P3 response in *Dictyostelium* cells. *Biophys. J.* 87:3764–3774.
40. Slepchenko, B. M., J. C. Schaff, J. H. Carson, and L. M. Loew. 2002. Computational cell biology: spatiotemporal simulation of cellular events. *Annu. Rev. Biophys. Biomol. Struct.* 31:423–441.
41. Iijima, M., and P. Devreotes. 2002. Tumor suppressor PTEN mediates sensing of chemoattractant gradients. *Cell.* 109:599–610.
42. Funamoto, S., R. Meili, S. Lee, L. Parry, and R. A. Firtel. 2002. Spatial and temporal regulation of 3-phosphoinositides by PI 3-kinase and PTEN mediates chemotaxis. *Cell.* 109:611–623.
43. Leslie, N. R., and C. P. Downes. 2004. PTEN function: how normal cells control it and tumour cells lose it. *Biochem. J.* 382:1–11.
44. Marshall, J. G., J. W. Booth, V. Stambolic, T. Mak, T. Balla, A. D. Schreiber, T. Meyer, and S. Grinstein. 2001. Restricted accumulation of phosphatidylinositol 3-kinase products in a plasmalemmal subdomain during Fc gamma receptor-mediated phagocytosis. *J. Cell Biol.* 153:1369–1380.
45. Arrieumerlou, C., and M. Meyer. 2005. A local coupling model and compass parameter for eukaryotic chemotaxis. *Dev. Cell.* 8: 215–227.